Electrochemistry Communications 186 (2026) 108156

Contents lists available at ScienceDirect

Electrochemistry Communications

journal homepage: www.elsevier.com/locate/elecom

Distortion-aware physics-based impedance modeling of commercial Li-ion batteries under non-ideal excitation signals

Xiaoxuan Chen [a,*], Dmitri L. Danilov [a,b,**], Tobias Frahm [c], Florian Rittweger [c], Thorben Schüthe [c], Karl-Ragmar Riemschneider [c], Yonggang Hu [d], Tim-Andy Benning [e], Johannes Thielmann [f], Luc H.J. Raijmakers [a], Rüdiger-A. Eichel [a,g]

[a] Forschungszentrum Jülich GmbH, Institute of Energy Technologies (IET-1), D-52425 Jülich, Germany
[b] Eindhoven University of Technology, Eindhoven 5600 MB, the Netherlands
[c] Hamburg University of Applied Sciences, D-20099 Hamburg, Germany
[d] Department of Chemistry College of Chemistry and Chemical Engineering, Xiamen University, Xiamen 361005, China
[e] Dräxlmaier GmbH, 84137 Vilsbiburg, Germany
[f] Infineon Technologies AG, 85579 Neubiberg, Germany
[g] RWTH Aachen University, D-52074 Aachen, Germany

ARTICLE INFO

Keywords:
Commercial lithium-ion batteries
Electrochemical impedance spectroscopy
Pseudo-two-dimensional (P2D) model
Parameter estimation
Frequency-domain parameter sensitivity analysis
Distorted excitation signals
Noise/clipping reconstruction

ABSTRACT

Electrochemical impedance spectroscopy (EIS) provides a sensitive probe for investigating internal physicochemical processes in lithium-ion batteries and has been widely considered for diagnostic applications. However, impedance measurements obtained under practical conditions are often affected by non-ideal excitation signals, environmental noise, and systematic distortions, which complicate the interpretation of EIS data using physics-based electrochemical models.

In this study, a distortion-aware framework is developed for physics-based impedance modeling of commercial 21,700 lithium-ion batteries. A pseudo-two-dimensional (P2D) model with double-layer capacitance is employed to simulate impedance responses over a broad frequency range. A frequency-resolved parameter sensitivity analysis is conducted to quantify the contributions of key electrochemical parameters across the impedance spectrum and to identify the dominant factors governing different frequency regimes.

Building on this sensitivity analysis, the model is further evaluated under realistic measurement conditions. Ambient noise and waveform distortions are identified through hardware impedance testing, reconstructed as biased excitation inputs, and processed using an FFT-based approach to extract impedance spectra from time-domain signals.

The model shows excellent agreement with experiments in both the DC and AC validation sets. Under low-rate discharge conditions (0.1C), the simulated voltage profile matches the experimental response, with an RMSE of 0.0423 V, and most deviations occur near the end-of-discharge knee at very low SoC. For impedance validation, the model reproduces the measured spectra with RMSE values of 0.282 mΩ and 0.224 mΩ for the real and imaginary parts, respectively. Under distorted excitations, including non-sinusoidal waveforms, Gaussian noise, and clipping, the median complex least-squares (CLS) error stays stable between 0.330 and 0.367 mΩ, and the maximum CLS error remains below 0.49 mΩ.

This work provides a practical methodology for interpreting impedance spectra of commercial lithium-ion batteries when signal distortions and noise cannot be neglected.

1. Introduction

Electrochemical impedance spectroscopy (EIS) provides critical insights into battery state and failure mechanisms, making it a valuable measurement technique for battery management systems (BMSs) [1]. Despite its potential, implementing EIS in electric vehicles (EVs) remains

* Corresponding author.
** Corresponding author at: Forschungszentrum Jülich GmbH, Institute of Energy Technologies (IET-1), D-52425 Jülich, Germany.
E-mail addresses: x.chen@fz-juelich.de (X. Chen), D.Danilov@tue.nl (D.L. Danilov).

https://doi.org/10.1016/j.elecom.2026.108156
Received 4 February 2026; Received in revised form 19 March 2026; Accepted 24 March 2026
Available online 25 March 2026

challenging due to practical limitations in signal generation, measurement accuracy, and model-based interpretation [2–5].

A first challenge lies in the excitation requirements. Laboratory EIS measurements typically rely on small-amplitude sinusoidal perturbations to ensure a linear response over a broad frequency range [6,7]. In onboard environments, however, excitation currents generated by power electronics often deviate from ideal sinusoidal waveforms because switching devices such as MOSFETs and IGBTs naturally operate in discrete states [8,9]. As a result, pulse-type or distorted excitations are more realistic in EV applications, complicating impedance estimation under non-ideal input conditions. Meanwhile, there is increasing interest in using EIS for battery state estimation in BMS applications. Data-driven approaches, especially those based on machine learning, have shown promising capabilities in predicting impedance behavior across different SOC and temperature conditions [10]. However, their performance often depends on sufficiently large datasets, and their generalization under realistic operating conditions remains challenging.

In addition, the interpretation of EIS data is fundamentally limited by the non-uniqueness of impedance models and the relatively low chemical specificity of electrochemical signals [11]. As a result, recent studies have explored hybrid approaches that combine physics-based modeling with data-driven methods to improve robustness and predictive capability [12]. In this context, reliably extracting physically meaningful parameters under non-ideal conditions becomes a key prerequisite.

A second difficulty is obtaining reliable voltage responses at the cell level. High-capacity automotive cells exhibit extremely low internal resistance, leading to voltage perturbations on the order of millivolts under typical EIS excitation currents. Such small signals are highly susceptible to electromagnetic interference and measurement noise. In addition, analog front-end amplification may introduce systematic distortions, including offset, phase shift, or clipping. These factors make impedance extraction increasingly unreliable when excitation signals are distorted or contaminated by noise [13–15].

A third challenge is the interpretation of impedance data using models suitable for diagnostic purposes. Equivalent circuit models (ECMs) are computationally convenient but often lack direct links to diffusion, kinetics, and aging-related physicochemical parameters [16]. Physics-based models such as the Pseudo-Two-Dimensional (P2D) model, derived within the seminal Doyle–Fuller–Newman (DFN) framework, provide a holistic description of transport and interfacial reactions [17,18]. However, parameter identification remains nontrivial due to the large number of coupled parameters and the difficulty of relating time-domain electrochemical dynamics to frequency-domain impedance responses [19–21].

To bridge this gap, two main modeling strategies have been explored. Nonlinear electrochemical impedance spectroscopy (NLEIS) directly analyzes higher-order harmonic responses under nonlinear perturbations [22–24], but its application is often limited by long simulation times at low frequencies. Alternatively, linearized frequency-domain approaches transform physics-based models around equilibrium points using Fourier or Laplace techniques and have been successfully applied in parameter estimation studies [25,26]. Several studies have demonstrated the potential of physics-based impedance modeling for mechanistic interpretation. For instance, Chang et al. optimized a DFN model directly from impedance spectra and achieved good agreement across a wide frequency range [27]. Zhang et al. investigated parameter sensitivities across different state-of-charge windows using a reduced-order electrochemical model [28]. In addition, Wimarshana et al. employed multi-step identification strategies that combined impedance data with heuristic optimization methods, such as particle swarm optimization [29]. These efforts highlight the promise of physics-based EIS modeling while underscoring the remaining challenges posed by non-ideal excitations and measurement distortions in practical environments.

Nevertheless, practical impedance estimation in EV-relevant conditions must account for waveform distortions, noise contamination, and unavoidable signal-processing artifacts in real measurements. Addressing these issues is essential for improving the robustness and interpretability of impedance-based diagnostics beyond ideal laboratory settings.

Here, we develop a physics-based impedance modeling framework to improve the reliability of EIS interpretation under non-ideal excitation conditions. The proposed approach combines: (i) a frequency-resolved parameter sensitivity analysis to quantify how key electrochemical parameters contribute across different frequency ranges; (ii) distortion-aware excitation reconstruction based on hardware impedance testing, enabling realistic noise and waveform imperfections to be incorporated into simulations; and (iii) FFT-based impedance extraction from time-domain voltage and current signals under non-sinusoidal, noisy, and clipped inputs. The framework is validated against experimental EIS data from commercial lithium-ion cells and demonstrates stable impedance prediction performance across a range of realistic excitation scenarios, providing a foundation for future integration with data-driven methods by enabling robust extraction of physically meaningful parameters under realistic conditions.

2. Time-domain model development

The impedance simulations in this work are based on the classical Doyle–Fuller–Newman pseudo-two-dimensional (P2D) framework, with several standard adaptations reported in the literature [30–32]. Throughout this paper, the subscripts “1” and “2” are used to distinguish between the solid and electrolyte phases, respectively. Variables with subscript 1 (e.g., φ_1 and i_1) refer to the electronic potential and current density in the solid electrode matrix, while variables with subscript 2 (e.g., φ_2 and i_2) represent the ionic potential and current density in the electrolyte phase. The interfacial potential difference $\varphi_1 - \varphi_2$ corresponds to the double-layer overpotential that governs charge-transfer and capacitive processes at the electrode–electrolyte interface. Following the corrected electrolyte charge conservation form, the transference-number multiplier in the electrolyte current balance is written as $(1 2t_+)$ rather than the conventional $(1t_+)$. Interfacial double-layer dynamics are further accounted for by introducing a capacitive contribution of the form $\frac{C_{dl}\partial(\varphi_1-\varphi_2)}{\partial t}$, which allows the model to capture short-time voltage relaxation effects relevant to impedance response. For the numerical implementation, the interfacial potential difference is expressed through $\varphi_1 - \varphi_2$, which corresponds to the double-layer overpotential. Since φ_1 and φ_2 enter the interfacial charge-transfer and capacitive relations primarily through their difference, this reformulation provides an equivalent, more compact representation of the coupled potential equations. The resulting governing equations and parameter definitions employed in this study are summarized in the Supplementary Information (Tables S1 and S2).

3. Experimental and methodology

3.1. Full-cell teardown and half-cell assembly

This work used commercial 21,700-type cylindrical batteries (MoliCel INR-21700-P45B) with $LiNi_{0.8}Co_{0.15}Al_{0.05}O_2$ (NCA)/graphite-SiO_x chemistry for cycling and EIS testing. Before disassembly, standard EIS measurement (10 mHz–10 kHz, with an AC amplitude of 5 mV) was conducted on the two individual cells at various SoCs to evaluate their consistency. The results are presented in Fig. S1. Next, the following procedure was used to extract the individual electrodes and assemble half-cells for open-circuit potential (OCP) measurements and subsequent electrode-balancing analysis. A whole cell was fully discharged to 2.5 V before disassembling in an argon-filled glove box with H_2O and O_2 concentrations lower than 0.1 ppm (ppm). A pipe-cutting tool was used to remove the lid along the perimeter of the cell's top. The steel cell can was carefully opened and removed with pliers until the jelly roll was fully exposed, after which it was unrolled and separated. The electrode

sheets (anode and cathode) were trimmed into pieces with approximately 30 cm in length. Both sheets were rinsed multiple times with fresh diethyl carbonate (DEC) over 15 min to remove residual electrolyte. The active material on one side of the coated electrodes was removed from the current collector using acetone to prepare single-layer material sheets. The electrodes were subsequently punched into 15 mm diameter disks. Coin-type half-cells were assembled by first placing the electrode disks into the cell cases, then adding a glass microfiber separator soaked in a 1.0 M $LiPF_6$ electrolyte dissolved in a 1:1 (wt/wt) mixture of ethylene carbonate (EC) and dimethyl carbonate (DMC). Lithium metal was used as the counter electrode. A stainless-steel spacer and a spring were added to ensure good contact, and the cells were sealed with coin-cell caps under proper pressure.

3.2. Electrode balancing

To obtain the quasi-open-circuit voltage (q-OCV) curve of the full cell and the quasi-open-circuit potential (q-OCP) curves of the electrodes, galvanostatic charging at a very low current rate (0.01C) was performed from 2.5 V to 4.2 V on both the full cell and the corresponding coin-type half-cells. All measurements were carried out at 25 °C in a temperature-controlled chamber. The OCPs of the cathode (NCA) and anode (graphite–SiO_x composite) are denoted as $V_p(s_p)$ and $V_n(s_n)$, respectively, where s_p and $s_n \in [0,1]$ represent normalized lithium stoichiometries, in the positive and negative electrodes, accordingly. The full-cell voltage as a function of *SoC* is therefore expressed as:

$$\mathrm{OCV}_{cell}(soc) = V_p\big(s_p(soc)\big) - V_n\big(s_n(soc)\big), \tag{1}$$

where *soc* is *SoC* of the battery at some moment in time. The stoichiometry–SoC mapping is defined as:

$$\begin{cases} s_p(soc) = s_p^{max} - \left(s_p^{max} - s_p^{min}\right) \bullet soc, \\ s_n(soc) = s_n^{min} + \left(s_n^{max} - s_n^{min}\right) \bullet soc. \end{cases} \tag{2}$$

Three empirical parameters characterizing the electrode matching, namely, the loading ratio (LR), *SoC* offset (OFS), and ohmic resistance increase (ORI), are further introduced [33–35] and identified by minimizing the error between the modeled and measured OCV–SoC curves. A Particle Swarm Optimization (PSO) algorithm, implemented in Python 3.8 via the *pyswarm* library (v1.3.0), was used to iteratively adjust the electrode OCP scaling parameters such that the difference $V_p(s_p) - V_n(s_n)$ closely matched the experimentally measured full-cell OCV. The cost function, minimized by the PSO, is defined as:

$$\mathscr{L}(\boldsymbol{\theta}) = \frac{1}{M}\sum_{i=1}^{M}\left[\mathrm{OCV}_{\exp}(soc_i) - \left(V_p\big(s_p(soc_i;\boldsymbol{\theta})\big) - V_n\big(s_n(soc_i;\boldsymbol{\theta})\big) - V_{ohm}\right)\right]^2, \tag{3}$$

where $\boldsymbol{\theta} = \left\{s_p^{min}, s_p^{max}, s_n^{min}, s_n^{max}, \mathrm{OFS}, \mathrm{LR}, \mathrm{ORI}\right\}$ is the parameter vector explored by PSO. OCV_{exp} means the experimentally measured full-cell quasi-OCV as a function of normalized SoC values soc_i. M is the number of SoC sampling points (e.g., 11 from 0% to 100%), and i is the specific sampling point. V_{ohm} is the voltage shift due to ohmic resistance. The OCP curves are interpolated using cubic splines to allow continuous evaluation. Convergence was assumed when the improvement in the cost function fell below 10^{-6} over 30 consecutive iterations.

3.3. Parameter sensitivity analysis based on QR decomposition

To evaluate the impact of each model parameter on the impedance output across a range of frequencies, a parameter sensitivity analysis was conducted. This analysis helps identify the parameters that most strongly influence the impedance response at a given frequency-dependent input, thereby guiding parameter selection, model simplification, and fitting strategies. For a given parameter vector p, the time-domain P2D equations are solved under an imposed excitation current $i(t)$, yielding the corresponding terminal voltage response $v(t;p)$. The complex impedance is then extracted in the frequency domain as,:

$$\widehat{Z}(f;p) = \frac{\widehat{V}(f;p)}{\widehat{I}(f)}, \tag{4}$$

where $\widehat{Z} = [\widehat{Z}(f_1), \widehat{Z}(f_2), \ldots, \widehat{Z}(f_N)]^{\mathrm{T}}$ is the calculated output value of impedance at each given frequency. $\widehat{V}(f)$ and $\widehat{I}(f)$ denote the Fourier transforms of the voltage and current signals, respectively. The parameters vector p affects the simulated impedance response through the numerical mapping $Z(f;p)$.

To quantify the sensitivity of each parameter on the impedance response, the Jacobian matrix $\boldsymbol{S} \in R^{N\times m}$ is computed as:

$$S_{kj} = \frac{\partial Z(f_k;p)}{\partial p_j} \tag{5}$$

where f_k represents the k-th frequency point and p_j denotes the j-th model parameter. Since $Z(f;p)$ is obtained numerically rather than from an explicit analytical expression, the derivatives are evaluated using a first-order finite-difference approximation. Each parameter is perturbed by a small relative increment $\Delta p_j = \epsilon p_j$ with $\epsilon = 10^{-3}$, and the Jacobian entries are computed as

$$S_{kj} = \frac{Z\left(f_k; p + \Delta p_j e_j\right) - Z(f_k;p)}{\Delta p_j}, \tag{6}$$

where e_j is the unit vector with 1 at the j-th position and zeros in all other places. This procedure provides a consistent frequency-resolved sensitivity measure without requiring an analytical impedance expression. The resulting Jacobian matrix serves as the basis for subsequent QR-based parameter ranking and contribution analysis across different frequency regimes.

3.4. Time-to-frequency domain transformation

Small-signal perturbations were introduced around a steady-state operating point, defined as a fully relaxed open-circuit condition at SoC = 50%, where no net current flows and the terminal voltage has stabilized. That ensures that the system remains linear and time-invariant during the perturbation analysis. On this basis, the governing equations were transformed into the frequency domain using Fast Fourier transform (FFT) for the impedance simulation. Eqs. (7) and (8) give the corresponding frequency-domain responses of current and voltage, respectively.

$$X_k = \sum_{n=0}^{N-1} I(t_n)\cdot e^{-j\frac{2\pi}{N}kn}, \tag{7}$$

$$Y_k = \sum_{n=0}^{N-1} \eta_W(t_n)\cdot e^{-j\frac{2\pi}{N}kn}, \tag{8}$$

where $I(t_n)$ and $\eta_W(t_n)$ are the discrete sequences of current and (over) voltage, while N is the number of samples and Δt is the time step.

The impedance $Z(\omega_k)$ as a function of frequency was computed as the ratio of the voltage and current components in the frequency domain, with $\omega_k = \frac{2\pi k}{N\Delta t}$. Taking the high-frequency (>10 kHz) inductive behavior into consideration, the final frequency-domain impedance output is calculated as:

$$Z(\omega_k) = \frac{Y_k}{X_k} + j\omega_k L, \tag{9}$$

where L is the equivalent (lumped) battery inductance.

3.5. Model implementation and settings

The model was implemented in MATLAB (R2024) based on a time-domain reparametrized P2D-DFN framework with double-layer capacitance. The governing equations were discretized using a finite-volume scheme along the through-plane direction, with 6, 3, and 6 control volumes assigned to the negative electrode, separator, and positive electrode, respectively. Solid-phase lithium diffusion in spherical active particles was resolved using 6 radial nodes in each electrode.

The resulting coupled differential–algebraic system was solved using Newton iterations with a fixed time step of 1 s and a solver tolerance of 10^{-3}. Spatial boundary conditions across the cell thickness were enforced via an iterative shooting-based procedure, in which the ionic current distribution was adjusted until the through-plane constraints converged. The electrolyte potential was subsequently recovered by integration, and the terminal voltage was evaluated accordingly.

Electrochemical impedance spectroscopy (EIS) simulations were performed by applying current excitations with an amplitude of 10 mA cm^{-2} over 18 logarithmically spaced frequencies from 0.1 Hz to 10^4 Hz. In addition to sinusoidal perturbations, triangular, sawtooth, and square waveforms were also considered. The impedance spectrum was extracted from the voltage response using FFT. A frequency-dependent inductance term was included to reproduce the high-frequency behavior observed experimentally.

3.6. Signal generation and hardware setup

Time-domain impedance spectra were obtained by applying controlled galvanostatic current excitations to cylindrical Molicel INR-21700-P45B cells. All measurements were performed in a temperature-controlled chamber at 25 °C. *Prior* to each test, the cell was rested for 2 h to ensure voltage stabilization at the targeted SoC.

Current excitations (50 mA peak) were generated by a function generator (Tektronix AFG1062) and applied via a power amplifier (Kepco BOP-5020MGL). The resulting terminal voltage and current responses were recorded with a sampling rate of 10 kHz.

Impedance spectra were subsequently reconstructed in the frequency domain using a fast Fourier transform (FFT)-based approach. The complex impedance was calculated as the ratio between the Fourier-transformed overvoltage response and the applied current excitation over the frequency range from 10 mHz to 10 kHz.

Non-ideal excitation distortions and acquisition errors encountered under realistic operating conditions are addressed separately in Section 4.4.

4. Results and discussion

4.1. OCP balancing and parameter calibration

The OCV of the full cell cannot be directly obtained by subtracting the anode OCP from the cathode OCP, as the SoCs of the two electrodes are not linearly correlated in practical systems. Instead, the SoCs must be aligned based on the negative-to-positive capacity (n/p) ratio and the operable voltage window. Herein, the full-cell OCV curve was reconstructed from individually measured electrode OCPs using a PSO-based balancing approach, as described in Section 3.3. Fig. 1(a) shows that the simulated OCV closely matches the experimental curve after tuning the electrode scaling parameters. The extracted $V_p(s_p)$ and $V_n(z)$ reflect the actual working windows of the positive and negative electrodes, respectively. To account for electrode mismatch and realistic cycling conditions, three key empirical parameters, LR, OFS, and ORI, characterizing the electrode matching, are identified through the reconciliation of the OCP and OCV curves. The balanced OCPs can improve simulation accuracy and ensure physically consistent input for frequency-domain analysis using the physics-based model. As impedance simulations are sensitive to electrode potentials, this step is essential for reliable EIS modeling. The incremental capacity (dQ/dV) and differential voltage (dV/dQ) analyses were further employed to verify the consistency between the modeled and experimental OCV curves, as shown in Fig. 1(b) and (c). Even when the differences between

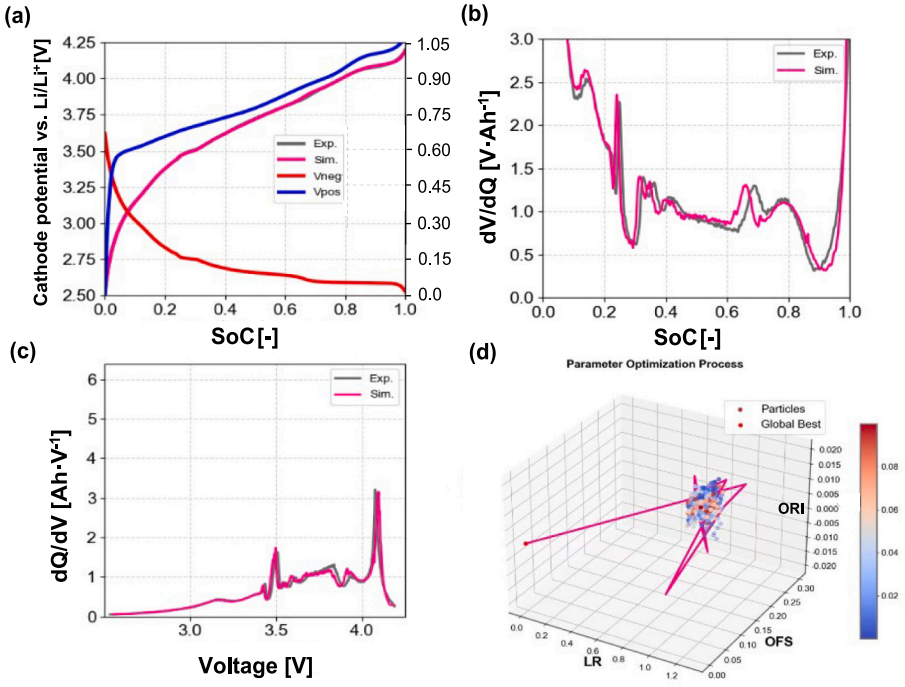

Fig. 1. Coin half-cell calibration based on particle swarm optimization for electrode balancing. (a) experimental (Exp.) and simulation results (Sim.) of full cell OCV curves and the balanced OCP curves of the cathode (V_p) and anode (V_n), respectively; The experimental and simulation OCV curves of (b) dV/dQ result as a function of SoC. (c) dQ/dV result as a function of voltage. (d) The convergence trajectory of particles (solutions) during the particle swarm optimization (PSO) process was used to fit the simulated OCV curve to the experimental data.

experimental data and the balanced OCV results are amplified by differential analyses, excellent agreement is still observed between the two, confirming the precise extraction of the electrode OCP curves. Fig. 1(d) visualizes the PSO optimization process in the LR-OFS-ORI parameter space. Particle convergence around the global best point indicates good optimization stability. According to the defined loss function in Eq. (3), the discrepancy between the simulated and experimental OCV remains within 1.5% across the entire SoC range.

4.2. Model validation in both time and frequency domains

The model parameter optimization and determination procedures are consistent with our earlier studies [36,37], and are therefore omitted here for brevity. Fig. 2 provides a validation of the proposed electrochemical model under both DC discharge and AC impedance conditions. In the time domain, Fig. 2(a) shows that the simulated voltage curve at 0.1C closely matches the experimental discharge profile over the full capacity range. The corresponding absolute voltage deviation $|\Delta V|$, plotted versus state of charge in Fig. 2(b), remains limited throughout most of the discharge process. After excluding the end-of-discharge region where the voltage drops sharply, the RMSE of the voltage prediction in the retained range is 0.042 V, indicating that the model reproduces the dominant discharge behavior with good accuracy.

Frequency-domain performance is evaluated using electrochemical impedance spectroscopy. As shown in Fig. 2(c), the simulated impedance spectra agree well with the experimental measurements in both Bode and Nyquist representations across the investigated frequency range. The model captures the main impedance features, including the high-frequency intercept and the mid-frequency arc response. The absolute errors of the impedance components are further quantified in Fig. 2(d), yielding RMSE values of 0.282 mΩ for the real part and 0.224 mΩ for the imaginary part. These sub-milliohm discrepancies confirm that the model provides accurate impedance predictions under small-signal AC excitation.

Overall, consistent agreement across discharge and impedance validations demonstrates that the proposed framework is sufficiently validated in both the time and frequency domains. This agreement establishes a reliable basis for the subsequent analysis of model performance under various realistic input signals and operating conditions.

4.3. Frequency-domain parameters sensitivity analysis

While parameter sensitivity analysis has been explored in previous studies, most of them focus on global or frequency-averaged behavior, without resolving how individual physical processes contribute at different time scales. To address this gap, we divide the impedance spectrum into three representative frequency regions: high-frequency (10 kHz–1034.1 Hz), mid-frequency (1034.1 Hz–4.17 Hz), and low-frequency (4.17 Hz–0.1 Hz). This frequency-resolved analysis enables a more nuanced interpretation of how physical processes, such as double-layer effects, charge transfer, and solid-phase diffusion, can shape the impedance response across different regimes.

Based on this frequency partitioning, we perform a sensitivity analysis using simulated EIS data. A Jacobian sensitivity matrix **S** was calculated according to Eqs. (5)–(6), and the QR decomposition was then applied to this matrix to rank the parameters by their relative influence.

Fig. 3 shows the parameter-ranking results obtained from the QR decomposition of the sensitivity matrix across different frequency regions. The decimal log scale was used to illustrate the behavior of sensitivities across the full range of parameters. To better visualize the contribution of the most influential parameters, each sensitivity plot also includes an inset showing the ranking curve on the natural scale. Across the whole range, as shown in Fig. 3(a), the cathode double-layer capacitance emerges as the most influential factor, followed by the cathode reaction rate constant, the anode charge transfer coefficient, and the anode active material volume fraction. When analyzing each frequency region individually, a clear shift in parameter importance is

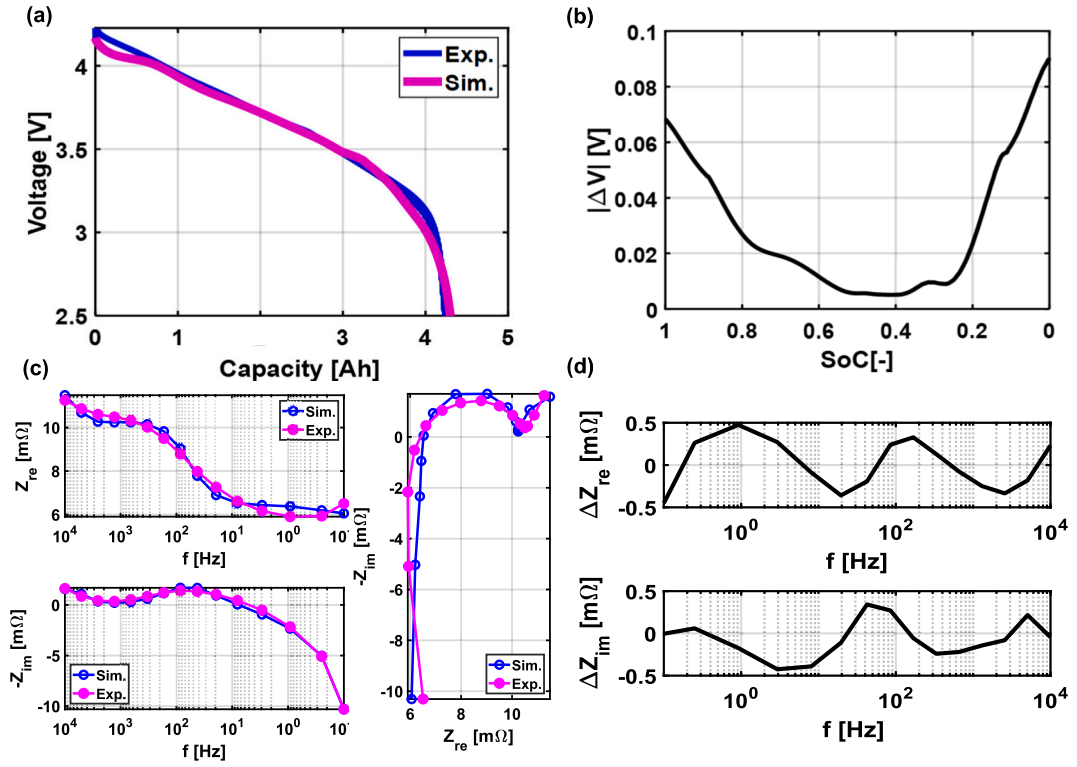

Fig. 2. Validation of the proposed model in the time and frequency domains. (a) Discharge voltage–capacity curves at 0.1C. (b) Absolute voltage error $|\Delta V|$ versus SoC. (c) Experimental and simulated impedance spectra in Bode and Nyquist forms. (d) Frequency-dependent absolute errors of Z_{re}(i.e.ΔZ_{re}) and Z_{im}(i.e.ΔZ_{im}).

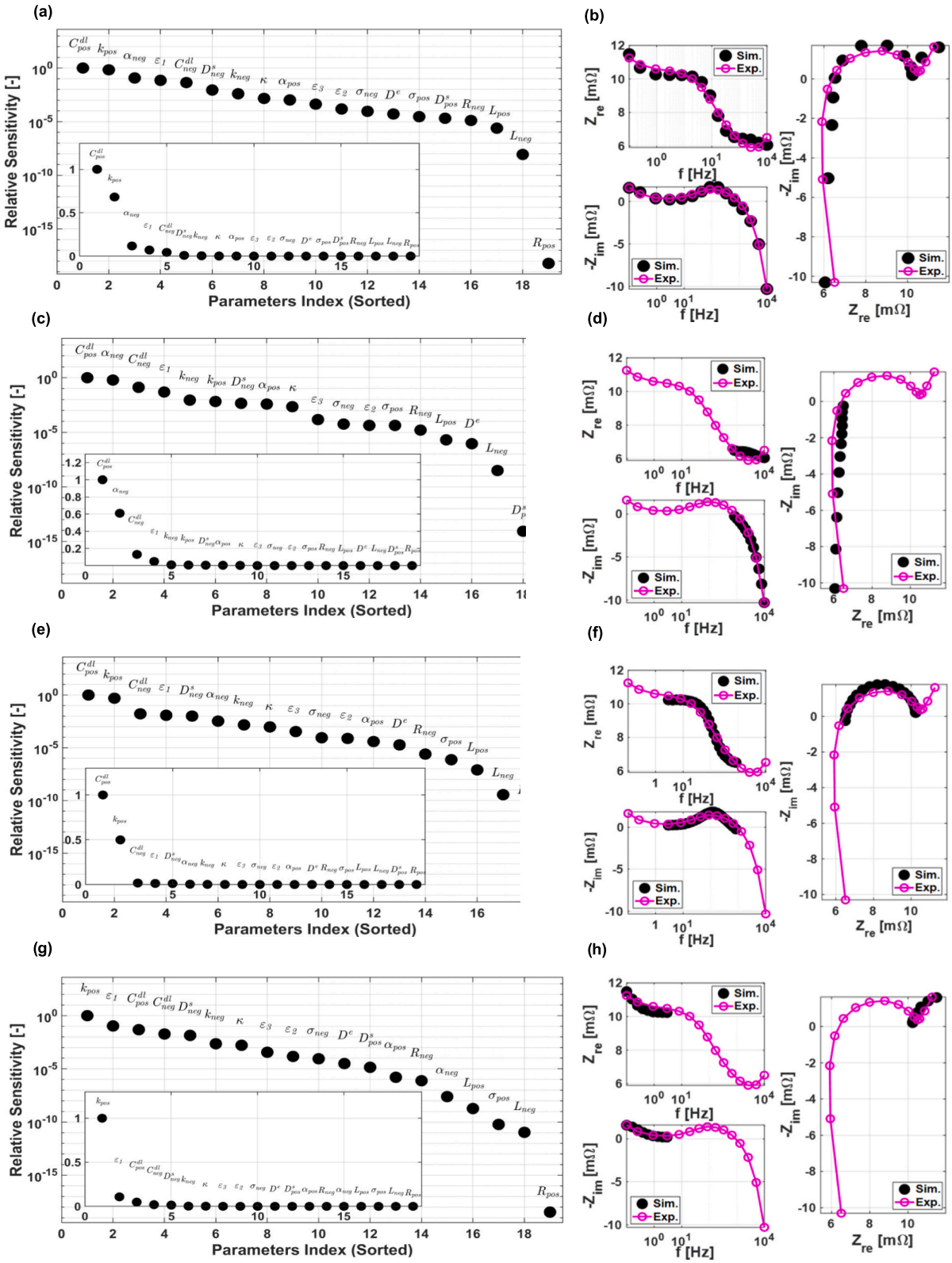

Fig. 3. Frequency-domain sensitivity analysis of the model parameters. (a), (c), (e), (g): QR-based sensitivity rankings given in the decimal log-scale: in the whole frequency range (a), high-frequency region (c), mid-frequency region (e), and low-frequency region (g), respectively. Insets show the same data in a natural scale to highlight low-sensitive parameters. (b), (d), (f), (h): Comparison of simulated and experimental impedance in the corresponding frequency regions. Left panels show the frequency dependence of the real and imaginary parts of impedance; right panels show the Nyquist plots.

observed, indicating transitions between interfacial- and transport-limited regimes. This decomposition provides valuable insight for both model interpretation and targeted experimental design.

In the high-frequency region, the top five most influential parameters remain the same as those identified across the full spectrum, albeit in a different order. That indicates that high-frequency dynamics strongly shape the overall impedance profile. In this regime, the cathode double-layer capacitance ranks first, followed by the anode charge transfer coefficient, highlighting the fast, interfacial nature of charge transfer at the electrode–electrolyte interface. The anode double-layer capacitance also exhibits high sensitivity due to its involvement in high-frequency polarization effects, surpassing other parameters such as porosity or reaction kinetics. The diffusion-related parameters have minimal impact in this region, as expected, since mass transport processes, particularly solid-phase ion diffusion, occur on slower time scales and thus contribute primarily at lower frequencies. Surprisingly, inductance does not rank among the top parameters here, although it is generally associated with the high-frequency behavior of the impedance spectrum. This unexpected result may stem from the specific model implementation or the relative numerical scaling of the inductance parameter and warrants further investigation.

As the frequency decreases into the mid-frequency region, the sensitivity landscape undergoes substantial changes. Fig. 3(e) shows that ion diffusion at the anode becomes significantly more influential, ranking among the top five parameters, indicating a transition from interface-dominated to transport-controlled behavior. Conversely, the charge transfer coefficient becomes less critical, while anode porosity remains among the top-ranked parameters. It reflects the increasing relevance of ion accessibility and pore structure in this frequency regime.

In the low-frequency region, the cathode reaction rate emerges as the dominant parameter, surpassing even the double-layer capacitance and diffusion processes. This result can be attributed to the slow electrochemical kinetics in porous electrodes, where reaction processes evolve over extended time scales and thus exert a greater influence on long-duration dynamics. At the same time, anode diffusion remains a key factor, indicating that both reaction and transport processes contribute significantly to the impedance response at low frequencies.

Table 1 illustrates the parameters ranked by sensitivity across all frequency regions considered. The content is derived directly from the QR-based sensitivity plots shown in Fig. 3. It is reorganized into a table format to facilitate easier side-by-side comparison and to highlight consistent trends across frequencies. This format allows more precise identification of consistently sensitive parameters, as well as those whose influence is frequency-dependent. Notably, the double-layer capacitance of both electrodes and the anode porosity consistently rank among the most sensitive parameters across all frequency regions, underscoring their foundational role in shaping the impedance response and the need for careful calibration in physics-based modeling.

Table 1
Model Parameter ranking from highest to lowest sensitivity across different frequency regions, based on QR decomposition of impedance simulation results.

Whole frequency region	High-frequency region	Mid-frequency region	Low-frequency region
C_{pos}^{dl}	C_{pos}^{dl}	C_{pos}^{dl}	k_{pos}
k_{pos}	α_{neg}	k_{pos}	ε_1
α_{neg}	C_{neg}^{dl}	C_{neg}^{dl}	C_{pos}^{dl}
ε_1	ε_1	ε_1	C_{neg}^{dl}
C_{neg}^{dl}	k_{neg}	D_{neg}^{s}	D_{neg}^{s}
D_{neg}^{s}	k_{pos}	α_{neg}	k_{neg}
k_{neg}	D_{neg}^{s}	k_{neg}	κ
κ	α_{pos}	κ	ε_3
α_{pos}	κ	ε_3	ε_2
ε_3	ε_3	σ_{neg}	σ_{neg}
ε_2	σ_{neg}	ε_2	D^{e}
σ_{neg}	ε_2	α_{pos}	D_{pos}^{s}
D^{e}	σ_{pos}	D^{e}	α_{pos}
σ_{pos}	R_{neg}	R_{neg}	R_{neg}
D_{pos}^{s}	L_{pos}	σ_{pos}	α_{neg}
$R_{neg}D_{pos}^{s}$	D^{e}	L_{pos}	L_{pos}
L_{pos}	L_{neg}	L_{neg}	σ_{pos}
L_{neg}	D_{pos}^{s}	D_{pos}^{s}	L_{neg}
R_{pos}	R_{pos}	R_{pos}	R_{pos}

Moreover, electrochemical reactions are increasingly constrained by diffusion and structural properties (e.g., porosity) at lower frequencies, whereas charge-transfer effects dominate at higher frequencies due to their faster interfacial kinetics. These trends confirm the expected transition from interface-controlled to transport-controlled behavior as the system shifts from short- to long-time dynamics.

4.4. Real-world applicability study of the model

In theory, the inherent impedance spectrum of a battery (in galvanostatic mode) is defined by the transfer function relating the overvoltage response $\eta(t)$ to the applied current excitation $I(t)$. Under ideal conditions, this relationship can be directly extracted from well-defined input-output pairs, yielding the inherent impedance.

However, practical impedance acquisition is inevitably affected by non-idealities originating from both the excitation source and the measurement electronics. As illustrated in Fig. 4, the applied current signal may deviate from the ideal excitation due to intrinsic disturbances introduced by real-world excitation hardware, including noise, signal distortion, and amplitude modulation. This excitation-side imperfection is represented as,

$$I_{app}(t) = I(t) + \xi_0(t), \tag{10}$$

where $\xi_0(t)$ denotes the aggregated ambient excitation error.

In addition, the digitization and acquisition process introduces further systematic distortions in both current and voltage measurements. Typical artifacts include quantization noise, offset drift, thermal noise, and clipping effects. To distinguish the affected signals, the measured overvoltage and current are expressed as:

$$\eta_{meas}(t) = \eta(t) + \xi_\eta(t), \tag{11}$$

$$I_{meas}(t) = I_{app}(t) + \xi_I(t), \tag{12}$$

where $\xi_\eta(t)$ and $\xi_I(t)$ represent the measurement error components in voltage and current, respectively. These disturbances cause deviations between the calculated and inherent impedances. To account for these effects in the modeling framework, the excitation disturbance $\xi_0(t)$ and the acquisition-related current distortion $\xi_I(t)$ were jointly considered as an overall disturbance added to the simulated input current. This approach enables evaluation of impedance behavior under non-ideal excitation conditions while preserving the electrochemical fidelity of the P2D model. The main noise sources and their influence on different impedance spectrum types are summarized in Table 2.

4.4.1. Input signal generation on the hardware

To evaluate the impact of different current excitation waveforms on measured voltage signals under realistic hardware conditions, three typical input signals, including sinusoidal, rectangular, and triangular, were individually applied to four Molicel INR-21700-P45B batteries using a programmable current source. The resulting terminal voltage was recorded via the onboard ADC of the measurement hardware. Figs. 5(a) and (b) show the measured current waveforms and voltage outputs. All signals were imposed at the same nominal amplitude (±5 A) and base frequency (0.1 Hz). This frequency range is sensitive to excitation distortion and signal conditioning effects. As shown in Fig. 5(a), the applied currents are affected by excitation side disturbances $\xi_0(t)$, originating from hardware limitations. The measured voltage responses in Fig. 5(b) further exhibit acquisition artifacts, including baseline drift,

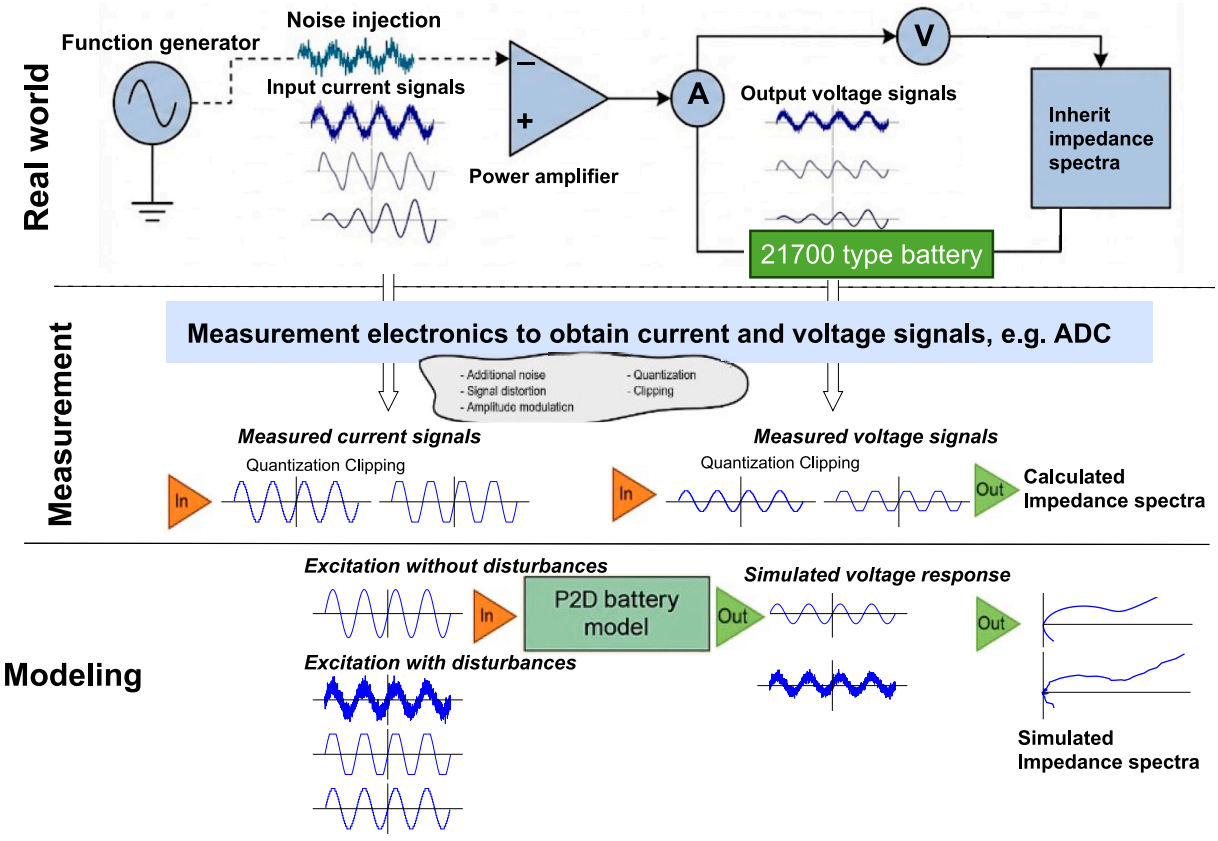

Fig. 4. Workflow for impedance measurement and modeling. Schematic overview of the differences from inherent real-world impedance, and comparing excitation sources, noise origins, measurement techniques, and resulting impedance outputs.

Table 2
Comparison of noise sources in different impedance spectra types.

Spectra type	Main noise sources	Mainly affects	Remarks
Inherent impedance spectra	Excitation source noise (e.g., ripple, jitter); battery intrinsic dynamics	Current	Voltage is a passive response; no clipping occurs.
Calculated impedance spectra	Measurement noise (e.g., ADC clipping, amplifier noise, quantization errors)	Voltage and current	Voltage is more sensitive due to a lower signal level; clipping may affect both.
Simulated impedance spectra	Manually introduced distortions in input; no physical noise	Current (by design)	Voltage is computed from the model; no measurement-induced noise is present.

noise, and clipping.

The case labeled 'sinusoidal 2' shows strong waveform asymmetry, consistent with amplifier saturation or ADC clipping. Such non-idealities can significantly degrade impedance accuracy, thereby motivating the disturbance-injection strategy introduced in Section 4.4.2.

These results highlight the importance of waveform selection and signal conditioning in practical impedance measurements. Electronic noise remains unavoidable in hardware-based acquisition.

4.4.2. *Input signal reconstruction in the software*

To evaluate the model's applicability under realistic operating conditions, representative current excitation waveforms were synthetically reconstructed based on experimentally acquired ADC signals (cf. Fig. 5 (a) and (b)). These signals, generated at a base excitation frequency of 0.1 Hz, were designed to closely mimic hardware-imposed constraints.

The ideal primary waveforms used in hardware tests are shown in Fig. 5(c) and exhibit consistent amplitude and frequency. Additional synthetic signals (e.g., sawtooth) are included for completeness in software reconstruction. To emulate hardware-induced distortions during signal acquisition, the ideal input signals were superimposed with zero-mean Gaussian noise at fixed signal-to-noise ratios (SNR). The signal-to-noise ratio γ is formally defined as:

$$\gamma = 20 \log_{10}\left(\frac{P_{signal}}{P_{noise}}\right), \tag{13}$$

where P_{signal} and P_{noise} are the signal and noise intensity, respectively. Fig. 5(d)–(f) represent resulting signals with γ equal to 10, 5, and 0. Such a choice illustrates increasing levels of measurement interference. While systematic bias can affect both current and overvoltage signals in practice, here the noise is applied only to the current input. This choice reflects two considerations. First, the current serves as the excitation signal and therefore directly influences the estimation of impedance. Second, in a used hardware setup, current signals are more prone to distortion due to switching effects and control limitations, whereas voltage measurements remain relatively stable. This approach enables pinpointing and evaluating the model's sensitivity to input-side degradation.

Additionally, Fig. 5(f) illustrates an extreme scenario ($\gamma = 0$) where the input signal is severely distorted by both high-intensity noise and waveform clipping. This case simulates additional disturbances from measurement electronics and clipping artifacts introduced by ADC limitations, as shown by the red line in Fig. 5(b). It reflects a practical situation in which excessive current amplification degrades the signal, a common issue in real-world systems. By constructing input signals with varying waveform types and noise levels, we create a controlled yet realistic framework to evaluate the model's robustness under imperfect

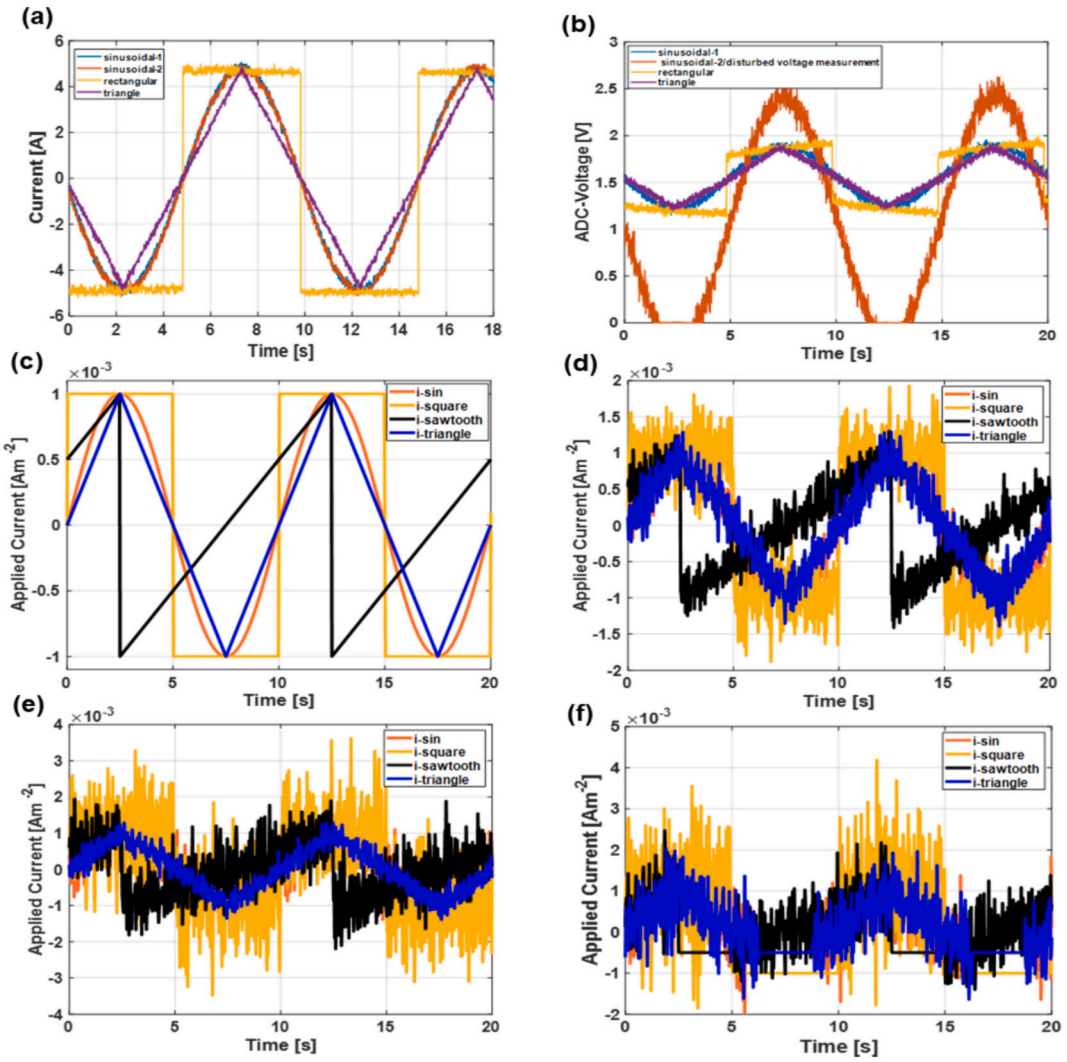

Fig. 5. Comparison of measured and simulated input signals. (a, b) Measured signals: (a) input current waveforms of various shapes (±5 A), and (b) corresponding ADC-recorded voltage signals, illustrating clipping in the 'sinusoidal 2' case due to amplification effects. (c–f) Simulated signals: (c) ideal waveforms; (d–f) corresponding waveforms with added Gaussian noise to achieve signal-to-noise ratios of 10 and 5. Panel (d) also includes simulated clipping to reproduce real-world disturbance effects. Simulated excitations were generated with a base frequency of 0.1 Hz.

signal conditions. Notably, although current is used as the excitation signal in this study, the same methodology and conclusions apply equally to voltage-controlled measurement schemes.

4.4.3. *Model validation under various realistic inputs*

Following the unified workflow shown in Fig. 4, the reconstructed excitations were sequentially applied to the P2D model for validation across waveform types and disturbance levels. Fig. 6 illustrates the complete workflow for evaluating the model's accuracy under various input current signal conditions. Using the ideal triangular waveform in Fig. 6(a) as an example, a single waveform type is sequentially applied at multiple discrete frequencies. This approach allows the assessment of the model's response over a broad frequency range under realistic excitation. Over the full frequency region, the model demonstrates near-perfect agreement with the experimental data. However, when zooming into specific sub-frequency regions (high, mid, low), small deviations become visible, indicating the model's sensitivity to localized error propagation.

To emulate realistic sensor environments, we further introduced artificial noise by superimposing controlled noise at signal-to-noise ratios $\gamma = 10, 5, 1, 0$, and by clipping the input current waveforms, as shown in Fig. 6(b). This process mimics measurement distortions typical of onboard vehicle electronics and environmental disturbance.

The impact of these noise levels on model accuracy was systematically quantified using the complex least squares (CLS) error metric, which is defined as the sum of squared relative differences in both the real and imaginary components of the impedance, calculated as follows,

$$\mathscr{L}_{CLS} = \sqrt{\frac{1}{K}\sum_{i=1}^{K}\left[\left(Z'_{sim,i} - Z'_{exp,i}\right)^2 + \left(Z''_{exp,i} - Z''_{sim,i}\right)^2\right]}, \tag{14}$$

where $Z'_{exp,i}$ and $Z''_{exp,i}$ are the real and imaginary parts of the experimental impedance at the i-th frequency point; $Z'_{mod,i}$ and $Z''_{mod,i}$ are the real and imaginary parts of the modeled impedance at the same frequency, respectively. K is the total number of frequency points in the dataset. Fig. 6(c) displays *violin plots* summarizing the error distributions across all tested waveform types and noise conditions. Despite increasing noise, the median error remained within approximately 0.330–0.367 mΩ range, with no significant increase. This observation demonstrates the model's robustness in suppressing ambient and systematic errors in the input signal and accurately recovering the inherent impedance spectrum. The ideal input signals, those with noise, and clipped input signals are shown in detail, and the results for other

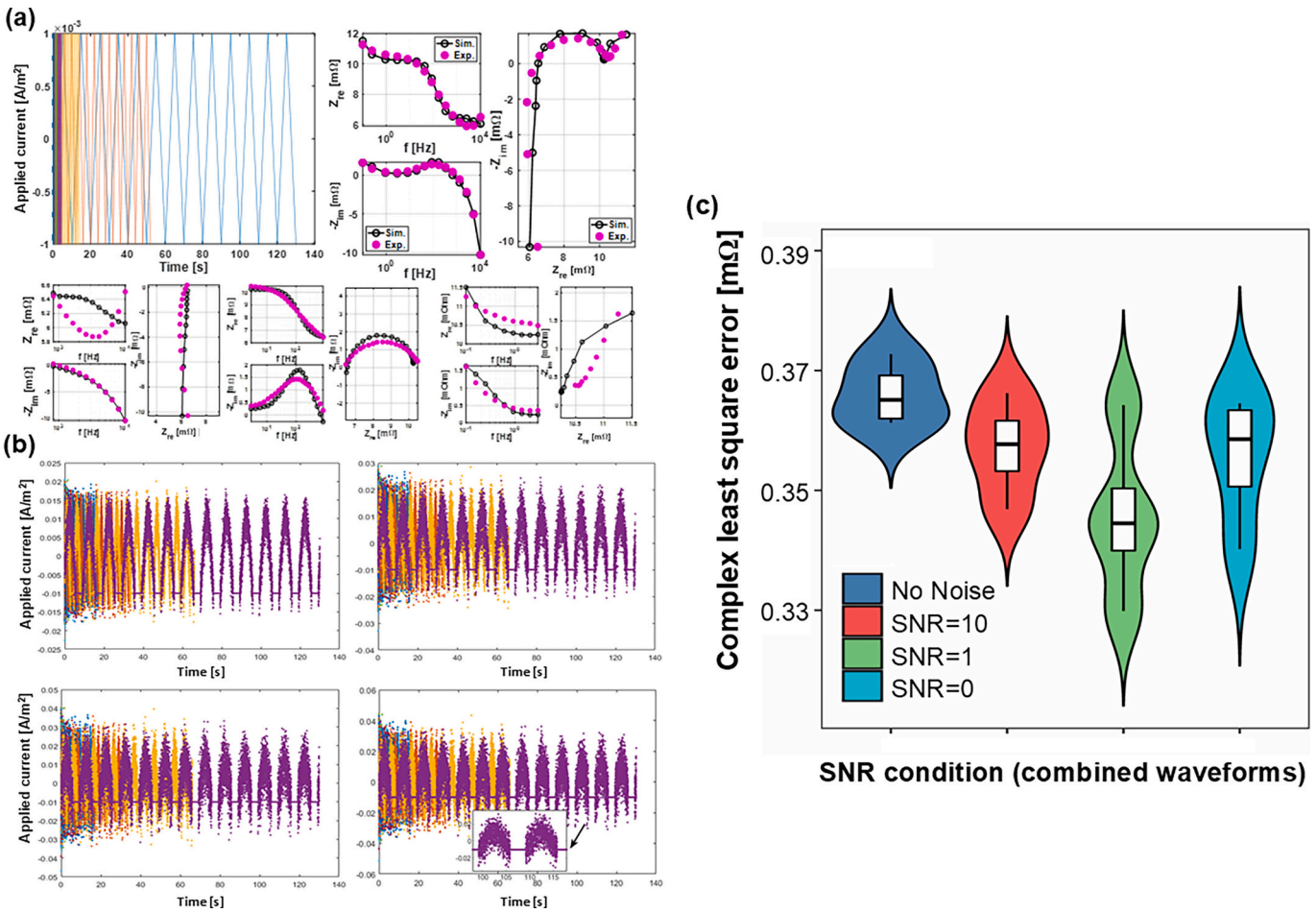

Fig. 6. Framework for assessing model performance with various input current signals. Sinusoidal, triangular, rectangular, and sawtooth waveforms were used as input signal shapes, with signal-to-noise ratios (SNR) of 10, 1, and 0 considered as representative noise cases for model evaluation. (a, b) Using the triangular waveform as an example, (a) shows, from left to right and top to bottom, the applied current signal at different frequencies, and the comparison between comparison between simulated impedance (Sim.) and experimental measurements (Exp.) (b) Simulated input signals with increasing noise levels: top left: SNR = 10; top right: SNR = 5; bottom left: SNR = 1; bottom left: SNR = 0. These waveforms reflect progressive signal degradation due to noise. (c) Violin plots showing the distribution of complex least-squares (CLS) errors under different SNR conditions. Each plot aggregates results across all waveform types (sinusoidal, square, triangular, and sawtooth) at a given noise level. The shaded area represents the kernel density estimate of the distribution. The internal rectangular box shows the interquartile range (IQR), with whiskers extending 1.5•IQR. The black line within the box indicates the median value.

waveforms (rectangular, square, and sawtooth) are provided in Figs. S2 and S3.

Fig. 7 presents a detailed evaluation of the model's performance under severe input signal distortions, including strong Gaussian noise ($\gamma = 0$) and waveform clipping across different frequency regions. Despite significant signal degradation, the model maintains high accuracy and robustness when compared with experimental impedance data.

In addition to the full-range comparison shown in Fig. 7(a), subplots Fig. 7(b)–(d) provide localized analyses across the ultra-high, mid-to-high, and low-frequency domains, respectively. The corresponding complex least-squares (CLS) error values are summarized in Table S4. These subplots confirm a strong agreement between the simulated and measured impedance responses under various noise and clipping conditions. The largest modeling error in the high-frequency region occurs when a sinusoidal input signal is combined with noise and clipping, yielding a CLS error of 0.4284 mΩ. In the mid-frequency region, the worst-case scenario is observed for the triangular waveform under similar conditions (0.3816 mΩ). In contrast, in the low-frequency region, the highest error arises with the noisy sawtooth input (0.3471 mΩ).

Notably, in the low-frequency region shown in Fig. 7(d), slight discrepancies emerge across various input signal distortions, particularly in regions associated with low solid-state diffusion or mass-transport limitations. This discrepancy is likely due to longer signal periods and limited averaging cycles, which increase the sensitivity to ambient drift and measurement noise, even though the voltage response magnitude is high due to increased impedance. The relatively small magnitude of the current response at low frequencies makes it more susceptible to external disturbances such as ambient temperature fluctuations and power supply noise. Overall, these results confirm the model's strong predictive performance and its resilience to non-ideal input excitations, highlighting its potential for practical impedance estimation applications in real-world BMS scenarios.

5. Conclusion

This work proposes a distortion-aware physics-based impedance modeling framework for commercial lithium-ion batteries under non-ideal excitation conditions. By combining a Newman-type P2D model with frequency-resolved sensitivity analysis, the study clarifies how interfacial kinetics and transport limitations shape regions of the impedance spectrum and supports a more targeted interpretation of parameters.

A key feature of the framework is the explicit incorporation of

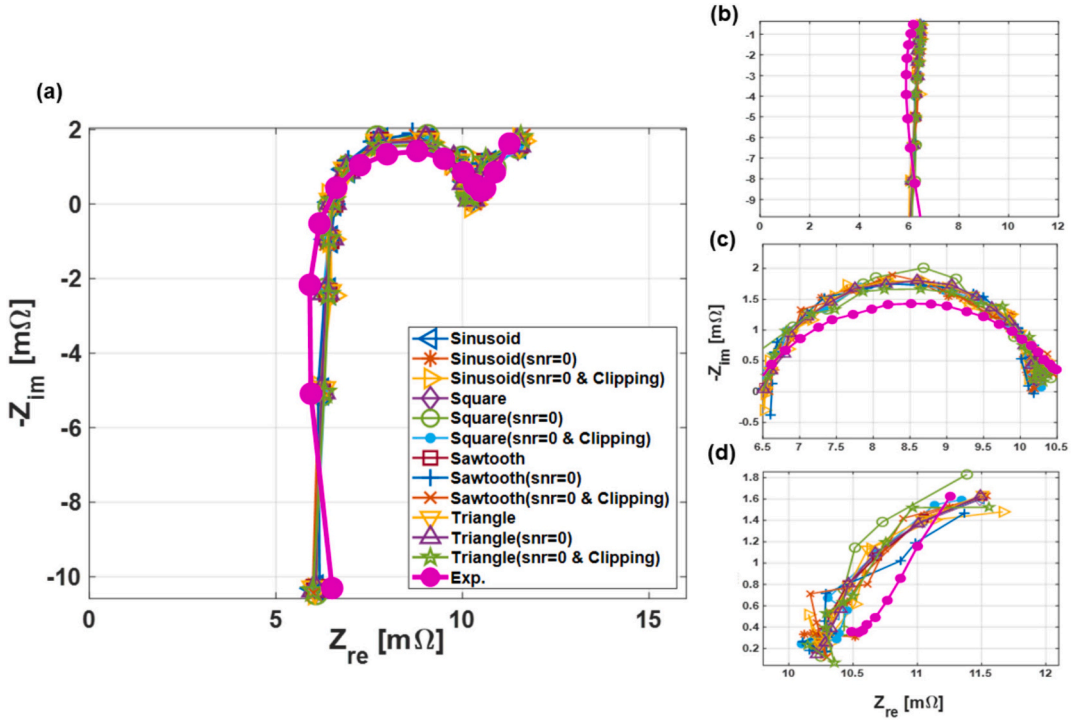

Fig. 7. Modeling results for different input waveforms and noise ratios, compared with experimental data across frequency regions. (a) Full frequency range; (b) high-frequency region; (c) middle-frequency region; and (d) low-frequency region.

realistic measurement distortions. Noise contamination, waveform deformation, and clipping effects observed during hardware testing are reconstructed as biased excitation inputs, thereby enabling impedance spectra to be evaluated under conditions that deviate from ideal laboratory assumptions. The results demonstrate that the model remains robust even when excitation signals are strongly distorted, providing reliable agreement with experimental spectra.

Future work will extend this approach to broader operating conditions, including temperature variation and aging-induced parameter drift, and further improve accuracy in the low-frequency regime where long relaxation processes remain challenging. The extracted parameters and their frequency-dependent sensitivities also provide a useful basis for future integration with data-driven approaches, such as machine learning, to investigate batteries.

Overall, the proposed methodology bridges mechanistic electrochemical modeling with practical impedance diagnostics, enabling a more realistic and robust interpretation of EIS measurements in commercial battery systems.

CRediT authorship contribution statement

Xiaoxuan Chen: Writing – original draft, Methodology, Investigation, Conceptualization. **Dmitri L. Danilov:** Writing – review & editing, Software, Conceptualization. **Tobias Frahm:** Validation, Investigation, Data curation. **Florian Rittweger:** Investigation, Data curation. **Thorben Schüthe:** Validation, Investigation. **Karl-Ragmar Riemschneider:** Supervision, Project administration. **Yonggang Hu:** Data curation. **Tim-Andy Benning:** Validation, Data curation. **Johannes Thielmann:** Validation, Data curation. **Luc H.J. Raijmakers:** Supervision, Resources, Funding acquisition. **Rüdiger-A. Eichel:** Supervision, Funding acquisition.

Declaration of competing interest

The authors declare that they have no known competing financial interests or personal relationships that could have appeared to influence the work reported in this paper.

Acknowledgments

This research is funded by the German Federal Ministry for Economic Affairs and Energy (BMWE) under grant number 03ETE046C. We sincerely express our gratitude to our project partners (BMW AG, Infineon Technologies AG, and Dräxlmaier GmbH), Hamburg University of Applied Sciences, the Center for Solar Energy and Hydrogen Research, and the Chair of Electrical Energy Storage Technology at the Technical University of Munich, for their invaluable insights and constructive discussions throughout the research process.

Appendix A. Supplementary data

Supplementary data to this article can be found online at https://doi.org/10.1016/j.elecom.2026.108156.

Data availability

Data will be made available on request.

References

[1] M. Gaberscek, Understanding Li-based battery materials via electrochemical impedance spectroscopy, Nat. Commun. 12 (1) (2021) 6513.
[2] W. Hu, et al., Application of electrochemical impedance spectroscopy to degradation and aging research of lithium-ion batteries, J. Phys. Chem. C 127 (9) (2023) 4465–4495.
[3] J. Huang, et al., Graphical analysis of electrochemical impedance spectroscopy data in Bode and Nyquist representations, J. Power Sources 309 (2016) 82–98.
[4] J. Huang, et al., An agglomerate model for the impedance of secondary particle in lithium-ion battery electrode, J. Electrochem. Soc. 161 (8) (2014) E3202–E3215.
[5] J. Huang, Correlation between electrocatalytic activity and impedance shape: a theoretical analysis, PRX Energy 3 (2) (2024).
[6] P. Shafiei Sabet, G. Stahl, D.U. Sauer, Non-invasive investigation of predominant processes in the impedance spectra of high energy lithium-ion batteries with nickel–cobalt–aluminum cathodes, J. Power Sources (2020) 472.
[7] A.C. Lazanas, M.I. Prodromidis, Electrochemical impedance spectroscopy-a tutorial, ACS Meas. Sci. Au 3 (3) (2023) 162–193.

[8] P. Gregory, Battery Management Systems, Volume I: Battery Modeling, Artech, 2015, p. 1.
[9] M. Kuipers, et al., An algorithm for an online electrochemical impedance spectroscopy and battery parameter estimation: development, verification and validation, J. Energy Storage (2020) 30.
[10] S. Temiz, et al., State of charge and temperature-dependent impedance spectra regeneration of lithium-ion battery by duplex learning modeling, J. Energy Storage 64 (2023) 107085.
[11] M.E. Orazem, B. Ulgut, Can interpretation of electrochemical impedance spectroscopy data be automated? Where do artificial intelligence algorithms stand? Curr. Opin. Electrochem. 55 (2026) 101788.
[12] Y. Che, et al., Mechanistically guided residual learning for battery state monitoring throughout life, Nat. Commun. 17 (1) (2026) 855.
[13] G.L. Plett, Extended Kalman filtering for battery management systems of LiPB-based HEV battery packs, J. Power Sources 134 (2) (2004) 252–261.
[14] X. Wang, et al., A review of modeling, acquisition, and application of lithium-ion battery impedance for onboard battery management, eTransportation (2021) 7.
[15] E. Quattrocchi, et al., A general model for the impedance of batteries and supercapacitors: the nonlinear distribution of diffusion times, Electrochim. Acta 324 (2019).
[16] S.E. Li, et al., An electrochemistry-based impedance model for lithium-ion batteries, J. Power Sources 258 (2014) 9–18.
[17] M. Doyle, T.F. Fuller, J. Newman, Modeling of galvanostatic charge and discharge of the lithium/polymer/insertion cell, J. Electrochem. Soc. 140 (6) (1993) 1526.
[18] T.F. Fuller, M. Doyle, J. Newman, Simulation and optimization of the dual lithium ion insertion cell, J. Electrochem. Soc. 141 (1994) 1–10.
[19] P. Hashemzadeh, et al., Investigation of the P2D and of the modified single-particle models for predicting the nonlinear behavior of Li-ion batteries, J. Energy Storage (2022) 52.
[20] A. Jokar, et al., Review of simplified Pseudo-two-dimensional models of lithium-ion batteries, J. Power Sources 327 (2016), p. 44-55.19.
[21] H.A.A. Ali, et al., A comparison between physics-based Li-ion battery models, Electrochim. Acta 493 (2024).
[22] N. Hallemans, et al., Electrochemical impedance spectroscopy beyond linearity and stationarity—a critical review, Electrochim. Acta 466 (2023).
[23] T.L. Kirk, et al., Nonlinear electrochemical impedance spectroscopy for lithium-ion battery model parameterization, J. Electrochem. Soc. 170 (1) (2023).
[24] M.D. Murbach, D.T. Schwartz, Extending Newman's pseudo-two-dimensional lithium-ion battery impedance simulation approach to include the nonlinear harmonic response, J. Electrochem. Soc. 164 (11) (2017) E3311–E3320.
[25] N. Wolff, et al., Nonlinear frequency response analysis on lithium-ion batteries: a model-based assessment, Electrochim. Acta 260 (2018) 614–622.
[26] L.A. Middlemiss, et al., Characterisation of batteries by electrochemical impedance spectroscopy, Energy Rep. 6 (2020) 232–241.
[27] C. Chang, et al., Electrochemical aging model of lithium-ion battery with impedance output and its parameter sensitivity analysis and identification, J. Energy Storage (2024) 86.
[28] Q. Zhang, et al., An electrochemical impedance model of lithium-ion battery for electric vehicle application, J. Energy Storage (2022) 50.
[29] B. Wimarshana, I. Bin-Mat-Arishad, A. Fly, A multi-step parameter identification of a physico-chemical lithium-ion battery model with electrochemical impedance data, J. Power Sources 580 (2023).
[30] F. Brosa Planella, W.D. Widanage, A single particle model with electrolyte and side reactions for degradation of lithium-ion batteries, App. Math. Model. 121 (2023) 586–610.
[31] A. Nyman, M. Behm, G. Lindbergh, Electrochemical characterisation and modelling of the mass transport phenomena in LiPF6–EC–EMC electrolyte, Electrochim. Acta 53 (22) (2008) 6356–6365.
[32] X. Chen, et al., State of health (SoH) estimation and degradation modes analysis of pouch NMC532/graphite Li-ion battery, J. Power Sources 498 (2021).
[33] M. Dubarry, et al., Identifying battery aging mechanisms in large format Li ion cells, J. Power Sources 196 (7) (2011) 3420–3425.
[34] M. Dubarry, B.Y. Liaw, Identify capacity fading mechanism in a commercial LiFePO4 cell, J. Power Sources 194 (1) (2009) 541–549.
[35] M. Dubarry, C. Truchot, B.Y. Liaw, Synthesize battery degradation modes via a diagnostic and prognostic model, J. Power Sources 219 (2012) 204–216.
[36] K. Chayambuka, et al., Physics-based modeling of sodium-ion batteries part I: experimental parameter determination, Electrochim. Acta 404 (2022).
[37] K. Chayambuka, et al., Physics-based modeling of sodium-ion batteries part II. Model and validation, Electrochim. Acta (2022) 404.